

A Principal Component Analysis of polycyclic aromatic hydrocarbon emission in NGC 2023

Ameek Sidhu^{1,2*}, Els Peeters^{1,2,3}, Jan Cami^{1,2,3} and Collin Knight¹

¹*Department of Physics & Astronomy, University of Western Ontario, London, ON, N6A 3K7, Canada*

²*Institute for Earth and Space Exploration, University of Western Ontario, London, ON, N6A 3K7, Canada*

³*SETI Institute, 189 Bernardo Avenue, Suite 100, Mountain View, CA 94043, USA*

ABSTRACT

We use the measured fluxes of polycyclic aromatic hydrocarbon (PAH) emission features at 6.2, 7.7, 8.6, 11.0 and 11.2 μm in the reflection nebula NGC 2023 to carry out a principal component analysis (PCA) as a means to study previously reported variations in the PAH emission. We find that almost all of the variations (99%) can be explained with just two parameters – the first two principal components (PCs). We explore the characteristics of these PCs and show that the first PC (PC_1), which is the primary driver of the variation, represents the amount of emission of a mixture of PAHs with ionized species dominating over neutral species. The second PC (PC_2) traces variations in the ionization state of the PAHs across the nebula. Correlations of the PCs with various PAH ratios show that the 6.2 and 7.7 μm bands behave differently than the 8.6 and 11.0 μm bands, thereby forming two distinct groups of ionized bands. We compare the spatial distribution of the PCs to the physical conditions, in particular to the strength of the radiation field, G_0 , and the G_0/n_H ratio and find that the variations in PC_2 , i.e. the ionization state of PAHs are strongly affected by G_0 whereas the amount of PAH emission (as traced by PC_1) does not depend on G_0 .

Key words: astrochemistry – infrared: ISM – ISM: lines and bands – ISM: molecules

1 Introduction

Polycyclic Aromatic Hydrocarbons (PAHs) are a large class of complex organic molecules made of carbon and hydrogen. They are strong absorbers of UV photons and release the absorbed energy mainly through vibrational modes in the mid-infrared (MIR) with dominant emission features at 3.3, 6.2, 7.7, 8.6, 11.2, and 12.3 μm (Sellgren et al. 1983; Leger & Puget 1984; Allamandola et al. 1985, 1989).

PAHs have been observed in a wide variety of astronomical environments via their characteristic emission features (e.g. Joblin et al. 1996; Sloan et al. 1999; Smith et al. 2007; Galliano et al. 2008). To first order, the PAH emission spectrum observed in diverse astronomical environments looks similar. However, there are subtle variations in relative intensities, peak positions, and profile shapes of the emission features depending on the environment in which they are observed (e.g. Hony et al. 2001; Peeters et al. 2002; Galliano et al. 2008). These variations are not only present between the different sources but also spatially within extended sources (e.g. Bregman & Temi 2005; Peeters et al. 2017; Boersma et al. 2018). Various experimental and theoretical studies suggest that the observed variations in the

PAH emission features are due to the changes in the properties of the PAH population such as the ionization state, size, and molecular structure (e.g. Allamandola et al. 1999; Bauschlicher et al. 2008, 2009; Ricca et al. 2012; Hony et al. 2001; Candian et al. 2014). The most prominent variations are observed in the ratio of 6.2, 7.7, and 8.6 μm bands to the 11.2 μm band, which are attributed to the changes in the ionization state of the PAHs (e.g. Allamandola et al. 1999; Galliano et al. 2008). Other observed variations include (but are not limited to) variations in the relative intensity of the short to long wavelength PAH bands (e.g. 3.3/11.2) associated with changes in the size distribution of the PAHs (e.g. Schutte et al. 1993; Ricca et al. 2012; Croiset et al. 2016; Knight et al. 2019), and variations in the relative intensity of the 11–14 μm PAH bands associated to the edge structure of the PAHs (e.g. Hony et al. 2001; Bauschlicher et al. 2008, 2009).

The observed changes in the characteristics of the PAH population are a result of the changing physical conditions such as density, strength of the UV radiation field, temperature, and metallicity of their residing environments. This clear dependence of PAHs on their local environment makes them a potential tool to probe the physical conditions. Galliano et al. (2008) and Boersma et al. (2015) used the variations in the ionization state of PAHs to develop a diag-

* E-mail: asidhu92@uwo.ca

nistic tool for tracing the physical conditions. These authors derived an empirical relation between the PAH ionization state (as traced by the 6.2/11.2 band ratio) and the so-called ionisation parameter, $\gamma = G_0 T^{1/2} / n_e$ where G_0 is the intensity of the radiation field in units of the average interstellar radiation field (the Habing field = 1.6×10^{-3} erg cm $^{-2}$ s $^{-1}$), T the gas temperature, and n_e the electron density. Recently, [Filleri et al. \(2012\)](#) discovered a strong anti-correlation between G_0 and the fraction of carbon locked up in evaporating small grains (eVSGs). In addition, [Stock & Peeters \(2017\)](#) reported a relation between G_0 and the 7.8/7.6 PAH band ratio in Galactic H II regions and reflection nebulae. Although a great deal of work has thus been done to explore the relationships between the PAH variability and the characteristics of their environments, the precise nature of this relationship is not clear yet.

In this work, we use a statistical approach to investigate the variations in the major PAH emission features in the well-known reflection nebula NGC 2023. We perform a Principal Component Analysis (PCA) of a set of fluxes of five major PAH bands at 6.2, 7.7, 8.6, 11.0, and 11.2 μ m to obtain the major driving factors of the observed variations in the PAH emission seen in NGC 2023. The paper is organized as follows. We describe the reflection nebula NGC 2023 in Section 2. In Section 3, we briefly summarize the key elements of a PCA. In Section 4, we present the results of our PCA of the PAH fluxes, followed by a discussion of PAH sub-populations in Section 5 and the peculiar behaviour of the ionic bands in Section 6. Finally, in Section 7, we discuss our results in the context of the physical conditions in the reflection nebula.

2 NGC 2023

NGC 2023 is a bright visual reflection nebula in the Orion constellation at a distance of 403 ± 4 pc ([Kounkel et al. 2018](#)). It is illuminated by the young B 1.5V star HD 37903, which carves out a dust-free cavity of ~ 0.05 pc around itself ([Witt et al. 1984](#)), and creates a photodissociation region (PDR) beyond that. For our analysis, we focus on the PAH emission observed in the PDR (e.g. [Sellgren 1984](#); [Abergel et al. 2002](#); [Peeters et al. 2012](#); [Shannon et al. 2016](#); [Boersma et al. 2016](#); [Stock et al. 2016](#); [Peeters et al. 2017](#); [Knight et al. 2019](#)).

We analyzed the MIR data obtained in the two regions of NGC 2023 (see Fig. 1), hereafter referred to as the north and the south field of view (FOV) respectively, with the Infrared Spectrograph (IRS [Houck et al. 2004](#)) in the Short-Low (SL) module (Spectral resolution ~ 60 -128, pixel scale $\sim 1.8''$), on board the Spitzer Space Telescope ([Werner et al. 2004](#)). The PDR surrounding the illuminating star has bright ridges, which are referred to as the southern ridge (S') at the top of the FOV, the southern ridge (S) in the middle of the FOV, the southeastern ridge (SE), and the south-southeastern ridge (SSE) in the south FOV and the north ridge (N) and the northwestern ridge (NW) in the north FOV as defined by [Peeters et al. \(2017\)](#). The north FOV is characterized by a gas density of $\sim 10^4$ cm $^{-3}$ ([Burton et al. 1998](#); [Steiman-Cameron et al. 1997](#); [Sandell et al. 2015](#)) and a radiation field of $\sim 10^3 G_0$ ([Burton et al. 1998](#); [Sandell et al.](#)

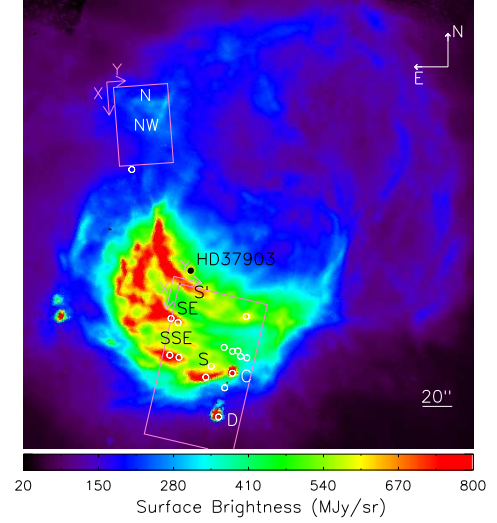


Figure 1. The IRAC [8.0] image of NGC 2023 with the IRS-SL fields of view (FOV) for the north and south regions shown as pink rectangles. The illuminating star HD 37903 is indicated by a black circle. The white circles represent 2MASS point sources, including sources C and D from ([Sellgren et al. 1983](#)), located inside the SL FOV. In the south FOV, there are four ridges, the southern ridge (S') at the top of the FOV, the southernmost ridge (S) in the middle of the FOV, the southeastern ridge (SE), and the south-southeastern ridge (SSE). In the north FOV, there are two ridges, the north ridge (N) and the northwestern ridge (NW). Figure is adapted from [Peeters et al. \(2017\)](#).

2015) which are lower as compared to a gas density of $\sim 10^5$ cm $^{-3}$ ([Steiman-Cameron et al. 1997](#); [Sheffer et al. 2011](#); [Sandell et al. 2015](#)) and a radiation field of $\sim 10^4 G_0$ ([Steiman-Cameron et al. 1997](#); [Sheffer et al. 2011](#)) in the south FOV.

3 Principal Component Analysis

A Principal Component Analysis (PCA) is a statistical technique for data visualization and dimensionality reduction developed by [Pearson \(1901\)](#) and [Hotelling \(1933\)](#). It transforms a set of correlated variables in a given data set into a new set of uncorrelated variables called the principal components (PCs) using an orthogonal transformation. The PCs are linear combinations of the original variables obtained in such a way that the first principal component has the largest variance and contains as much of the statistical information in the data as possible. Each succeeding component has a variance lesser than the preceding component thereby containing the remaining information in the data set. Thus, the goal of a PCA is to find the key variables that can best describe the data. A PCA can be applied to any dataset and is widely used in astronomy. A comprehensive review of PCA can be found in [Abdi & Williams \(2010\)](#) and [Jolliffe & Cadima \(2016\)](#).

Here, we briefly describe the underlying mathematical formalism of PCA. Consider a set of m variables $\{x_i\}$, measured from a set of n observations in the data set \mathbf{X} , an $n \times m$ matrix. As a first step, the raw data set, \mathbf{X} , is standardized such that each variable in the standardized data set, \mathbf{Z} , an $n \times m$ matrix, has a mean of zero and a unit

standard deviation. The standardization is done to ensure that all the variables have a comparable scale of measurement so that we get a more meaningful set of PCs. Next, we calculate the covariance matrix, \mathbf{C} , an $m \times m$ matrix, of the standardized dataset \mathbf{Z} . The covariance is a measure of the degree to which the two variables are correlated. It is zero for two independent variables and is equal to the variance when we calculate the covariance of a variable with itself. The covariance matrix has a set of m eigenvectors, $\{\mathbf{v}_1, \mathbf{v}_2, \dots, \mathbf{v}_m\}$, given by the linear combination of the standardized variables:

$$\mathbf{v}_i = a_{i,1}z_1 + a_{i,2}z_2 + \dots + a_{i,m}z_m \quad (1)$$

where $a_{i,j}$ are the coefficients of the eigenvector v_i and the $\{z_1, z_2, \dots, z_m\}$ are the set of original standardized variables. The corresponding set of m eigenvalues, $\{\lambda_1, \lambda_2, \dots, \lambda_m\}$, represents the variance of the eigenvectors (for the derivation, see Jolliffe & Cadima (2016)). Since the key objective of a PCA is to find a set of variables that successively maximizes the variance, the eigenvector corresponding to the largest eigenvalue of \mathbf{C} is called the first PC (PC_1), followed by the eigenvector corresponding to the second largest eigenvalue as the second PC (PC_2) and so on. Note that the covariance matrix, \mathbf{C} , is a symmetric matrix, so the eigenvectors corresponding to different eigenvalues are orthogonal and hence the principal components obtained are independent of each other.

The data set in the reference frame of the PCs can be obtained from the following equation:

$$\mathbf{Y} = \mathbf{AZ}^T \quad (2)$$

where the transpose of the matrix \mathbf{Y} (\mathbf{Y}^T) is a new data set in the reference frame of the principal components and \mathbf{A} is a transformation matrix given by

$$\mathbf{A} = \begin{bmatrix} a_{11} & a_{12} & \cdots & a_{1m} \\ a_{21} & a_{22} & \cdots & a_{2m} \\ \vdots & \vdots & \ddots & \vdots \\ a_{m1} & a_{m2} & \cdots & a_{mm} \end{bmatrix}$$

where the rows of the matrix correspond to the coefficients of the PCs determined from the eigenvalue decomposition of the covariance matrix \mathbf{C} , with the first row containing coefficients of PC_1 , the second row containing coefficients of PC_2 and so on.

4 PCA of PAH band fluxes in NGC 2023

4.1 Measurements of PAH bands

To determine the main parameters that drive the variability in the PAH fluxes in NGC 2023, we performed a PCA of the fluxes of five PAH bands at 6.2, 7.7, 8.6, 11.0, and 11.2 μm in the north and the south FOVs of the nebula. The flux values of these bands are taken from Peeters et al. (2017). We summarize their measurements here. Peeters et al. (2017) applied three different methods to measure the fluxes of the PAH bands. Here we use the band fluxes measured with the spline decomposition method. In this method, they subtracted a local spline continuum from the spectra and obtained the fluxes of the 6.2, 7.7, and 8.6 μm PAH bands by integrating the continuum subtracted spectra. The flux

measurements of the 11.0 and 11.2 μm bands, however, were done differently because of their blending with each other. To measure these fluxes, Peeters et al. (2017) fitted these bands with two Gaussians peaking at 10.99 and 11.26 μm with a FWHM of 0.154 and 0.236 μm respectively. The Gaussian at 10.99 μm provides the flux of the 11.0 μm band. To obtain the flux of the 11.2 μm band, they subtracted the flux of the 11.0 μm from the integrated flux of the 11.0 and 11.2 μm bands in the continuum-subtracted spectra (i.e. not using the Gaussian fit for the 11.2 μm band). Furthermore, the signal-to-noise ratios (SNR) of the PAH bands were estimated using the following expression:

$$SNR = \frac{I_{PAH}}{rms \times \sqrt{N} \times \Delta\lambda}$$

where I_{PAH} is the intensity of a PAH band in units of $\text{Wm}^{-2}\text{sr}^{-1}$, rms is the root-mean-square estimate of the noise, N is the number of spectral wavelength bins in the corresponding PAH band, and $\Delta\lambda$ is the wavelength bin size determined from the spectral resolution. Note that Peeters et al. (2017) take N as the number of data points in the corresponding PAH band. Since the Spitzer IRS data is oversampled by a factor of two, a discrepancy by a factor of $\sqrt{2}$ occurs in the SNR of the PAH band measurements in Peeters et al. (2017) dataset. Various studies show that the plateaus are distinct from the individual PAH bands perched on top of them (e.g. Bregman et al. 1989; Roche et al. 1989; Peeters et al. 2012, 2017). We have used the measurements of PAH bands from Peeters et al. (2017) that does not include plateaus. Therefore, for any other measurement of PAH bands that does not include plateaus we would expect change in the results smaller than that probed by the dynamic range of PCA.

The 6.2, 7.7, 8.6, and 11.0 μm bands are strong in charged PAH molecules whereas the 11.2 μm band is strong in neutral PAH molecules (e.g. Allamandola et al. 1999; Hony et al. 2001; Bauschlicher et al. 2008). In our analysis, we have used only the fluxes of the strongest PAH bands except for 11.0 μm , in order to have good quality measurements. We used the weaker 11.0 μm band because when normalized to 11.2 μm , it is a better tracer of the ionization state of PAHs than the other ionized PAH bands (e.g. Rosenberg et al. 2011; Peeters et al. 2017). The 11.0 μm band originates from the out of plane bending modes of solo C-H groups in ionized PAH molecules while the 11.2 μm originates from the same mode in neutral PAH molecules, thus the ratio 11.0/11.2 traces solely the ionization state of PAHs without any dependency on other parameters such as the size or the structure of molecule (e.g. Hudgins & Allamandola 1999; Hony et al. 2001; Bauschlicher et al. 2008, 2009). Moreover, for our analysis, we only included pixels where we have a 3σ * detection in *all* five PAH bands considered here and masked the remaining pixels. Following Peeters et al. (2017), we also masked the young stellar objects C and D (Sellgren et al. 1983). Note that we combined the measurements from the north and south FOVs for the PCA analysis discussed in this paper.

* Given the different SNR calculations in Peeters et al. (2017), our applied 3σ limit corresponds to a 4.2σ detection.

PAH band	$\langle I_{PAH} \rangle$ ($\times 10^{-6}$)	σ_{PAH} ($\times 10^{-6}$)
6.2	5.705	2.550
7.7	10.36	4.572
8.6	1.694	0.833
11.0	0.278	0.132
11.2	2.450	1.370

Table 1. The mean ($\langle I_{PAH} \rangle$) and standard deviation (σ_{PAH}) values of the PAH band flux variables. All values have units of $\text{Wm}^{-2}\text{sr}^{-1}$.

We standardized the PAH fluxes of the five bands considered here such that the standardized flux variables have a zero mean and a unit standard deviation

$$z_{PAH,i} = \frac{I_{PAH,i} - \langle I_{PAH} \rangle}{\sigma_{PAH}} \quad (3)$$

where $I_{PAH,i}$ is the intensity of a PAH band at pixel i , $\langle I_{PAH} \rangle$ and σ_{PAH} are the mean and standard deviation of the measured fluxes of a given PAH band, and $z_{PAH,i}$ is the corresponding standardized intensity. Table 1 lists the mean $\langle I_{PAH} \rangle$ and standard deviation σ_{PAH} values of the PAH flux variables in the nebula. The standardized variables (z_{PAH}) have comparable magnitudes and are the input variables in our PCA.

4.2 Principal Components

Our PCA resulted in five principal components (PCs). These PCs are linear combinations of the standardized flux variables (z_{PAH}). We note that the sign of a PC in PCA is arbitrary. Since we will be comparing the PCs (and especially the first two PCs), it makes sense to have them point in the same direction to facilitate interpretation. We thus choose to have the PC_1 and PC_2 vectors point in the direction of positive $z_{11.2}$ so that larger values of both PC_1 and PC_2 correspond to larger values of $z_{11.2}$ as well. With

PC	% variance explained
1	90.94
2	7.96
3	0.59
4	0.44
5	0.07

Table 2. Fraction of variance explained by the principal components (PCs).

that convention, the PCs are determined by the following expressions:

$$\begin{aligned}
 PC_1 &= 0.466 z_{6.2} + 0.467 z_{7.7} + 0.453 z_{8.6} \\
 &\quad + 0.444 z_{11.0} + 0.403 z_{11.2} \\
 PC_2 &= 0.106 z_{6.2} - 0.016 z_{7.7} - 0.349 z_{8.6} \\
 &\quad - 0.469 z_{11.0} + 0.804 z_{11.2} \\
 PC_3 &= -0.002 z_{6.2} - 0.288 z_{7.7} - 0.582 z_{8.6} \\
 &\quad + 0.741 z_{11.0} + 0.174 z_{11.2} \\
 PC_4 &= 0.461 z_{6.2} + 0.551 z_{7.7} - 0.567 z_{8.6} \\
 &\quad - 0.141 z_{11.0} - 0.378 z_{11.2} \\
 PC_5 &= 0.747 z_{6.2} - 0.629 z_{7.7} + 0.115 z_{8.6} \\
 &\quad - 0.121 z_{11.0} - 0.132 z_{11.2}
 \end{aligned} \quad (4)$$

where $\{z_{6.2}, z_{7.7}, z_{8.6}, z_{11.0}, z_{11.2}\}$ are the standardized flux variables.

Table 2 lists the fraction of the variance explained by the individual PCs. Clearly, the first two PCs combined account for the majority of the variation ($\sim 99\%$) present in the data. Since the last three PCs combined account for only 1% of the variation, we exclude those PCs from further analysis. Thus, in the framework of PCA dimensionality reduction, we can now decompose the standardized flux variables into PC_1 and PC_2 components:

$$\begin{aligned}
 z_{6.2} &= 0.466 PC_1 + 0.106 PC_2 \\
 z_{7.7} &= 0.467 PC_1 - 0.016 PC_2 \\
 z_{8.6} &= 0.453 PC_1 - 0.349 PC_2 \\
 z_{11.0} &= 0.444 PC_1 - 0.469 PC_2 \\
 z_{11.2} &= 0.403 PC_1 + 0.804 PC_2
 \end{aligned} \quad (5)$$

These equations include the directional choice discussed above.

Fig. 2 shows so-called “biplots” obtained from this PCA analysis that show the projection of the standardized original variables (z_{PAH}) onto the axes in the new reference frame defined by the PCs. Note that biplots are the visual representation of equation 5. The larger the projection of a variable on a PC axis, the better that variable correlates

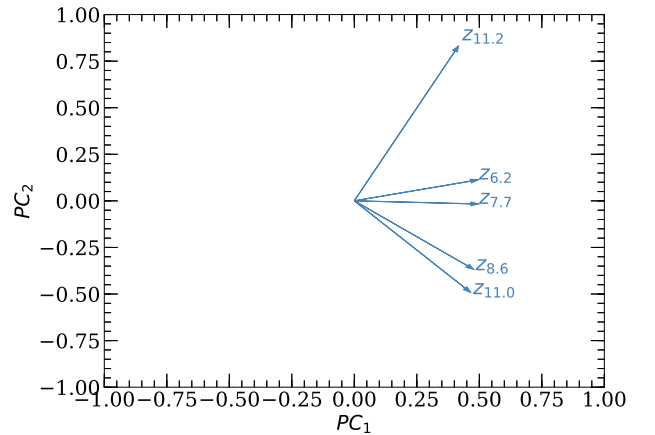


Figure 2. Biplots in PC_1 - PC_2 plane in NGC 2033. Biplots show the projection of the standardized flux variables onto the PC_1 and PC_2 axes.

with that PC. These biplots are thus useful tools to get a first idea about what drives variations in the original data set. We note that the projection of all z_{PAH} on PC_1 is in the positive direction indicating that PC_1 represents changes in total PAH flux. The magnitude of the projection of PC_1 is roughly the same for all the ionized flux variables ($z_{6.2}$, $z_{7.7}$, $z_{8.6}$, and $z_{11.0}$) but is relatively small for the neutral flux variable ($z_{11.2}$). This means that PC_1 has a slightly higher contribution from the ionized PAH bands than the neutral PAH band. Note also that $z_{7.7}$ is nearly horizontal in the biplot. Thus, PC_1 correlates almost perfectly with $z_{7.7}$, and $z_{7.7}$ is hardly affected by PC_2 .

Similarly, the projections of z_{PAH} on PC_2 provide a hint for the physical interpretation of PC_2 . The projection of $z_{11.2}$ and $z_{6.2}$ on PC_2 is in positive direction although the projection of $z_{6.2}$ is tiny as compared to that of $z_{11.2}$ while $z_{8.6}$ and $z_{11.0}$ project in the negative direction of PC_2 . The projection of $z_{7.7}$ is almost zero. Due to a clear distinction in the direction of the projection of $z_{8.6}$ and $z_{11.0}$ and $z_{11.2}$, PC_2 may be interpreted as a tracer of the ionization state of PAHs. However, in this scenario, the positive projection of $z_{6.2}$ is very intriguing and needs further investigation. At the same time, it is worth pointing out that the four ionic bands appear grouped in these biplots: $z_{6.2}$ and $z_{7.7}$ point in a similar direction, and also $z_{8.6}$ and $z_{11.0}$ point in a similar direction, but the two sets are quite distinct from each other. As will discuss later, this is the first evidence that points to a different character for a subset of the ionic bands.

4.3 Spectrum of PCs

Since PC_1 is a linear combination of PAH fluxes, the eigen vector corresponding to PC_1 represents a particular ratio of individual flux values, and thus a characteristic PAH spectrum. In Fig. 3, we show the characteristic PAH spectrum of PC_1 . This spectrum is derived from equation 5 by setting $PC_1 = 1$ and $PC_2 = 0$. From the values of the standardized flux variables thus obtained we then extract the actual flux values for the PAH bands by applying an inverse of the standardization operation i.e. adding the mean value of the original flux variables ($\langle I_{PAH} \rangle$) to the product of the standard deviation of the original flux variables (σ_{PAH}) and the standardized values obtained from equation

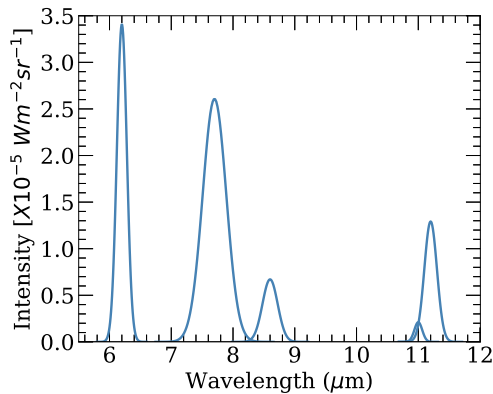


Figure 3. Characteristic PAH spectrum of PC_1 in NGC 2023. It is an artificial PAH spectrum created for the five PAH bands considered in the PCA (see text for details).

5 under the condition of $PC_1 = 1$ and $PC_2 = 0$. The spectrum is then constructed by representing each PAH band by a normalized Gaussian profile at its nominal peak position. Since the width of the observed PAH bands varies from one another, we constructed the Gaussians at 6.2, 7.7, 8.6, 11.0, and 11.2 μm with a standard deviations of 0.08, 0.19, 0.12, 0.07, 0.10 μm respectively. The 6.2 and 7.7 μm bands emerge as strong features. The 8.6 and 11.2 μm band also have considerable intensities, but significantly lower than those of the 6.2 and 7.7 μm bands. The 11.0 μm is the weakest feature because of its weak intrinsic intensity. Theoretical and experimental studies have shown that the spectra of ionized PAH molecules have strong 6.2, 7.7, and 8.6 μm bands whereas the spectrum of neutral PAH molecules have strong 11.2 μm band intensity with weak 6.2, 7.7, and 8.6 μm band intensities (e.g. Allamandola et al. 1999; Peeters et al. 2002; Bauschlicher et al. 2009). Thus, the characteristic PAH spectrum for PC_1 is neither a spectrum typical of solely cations nor solely neutrals but rather that of some mixture of cationic and neutral PAH molecules. The strong contribution from the 6.2, 7.7, and 8.6 μm bands as compared to the 11.2 μm in PC_1 suggest that PC_1 represents PAH emission of a mixture of PAH molecules where ionized PAHs outweigh the neutral PAHs.

In order to test our hypothesis and take into account the fact that the 6.2 and 7.7 μm bands have large intrinsic intensities that can manifest as strong features in the characteristic spectrum of PC_1 , we also constructed a spectrum using only the standardized values of the variables and a standard deviation of 0.1 μm – essentially the “eigen spectrum” corresponding to PC_1 – and show it in Fig. 4. We note that the eigen spectrum is representative of the eigen vector associated with the PC. In the eigen spectrum of PC_1 , the 6.2, 7.7, 8.6, and 11.0 μm bands have similar intensities, with the 11.2 μm band being slightly weaker. This implies that the 6.2, 7.7, 8.6, and 11.0 μm bands have larger contribution towards PC_1 as compared to the 11.2 μm band. Hence, our conclusion about PC_1 representing PAH emission of a mixture of PAH molecules having more ionized PAHs than the neutrals still holds.

We also derived an eigen spectrum of PC_2 . Since PC_2 represents a first order correction to the PAH fluxes pre-

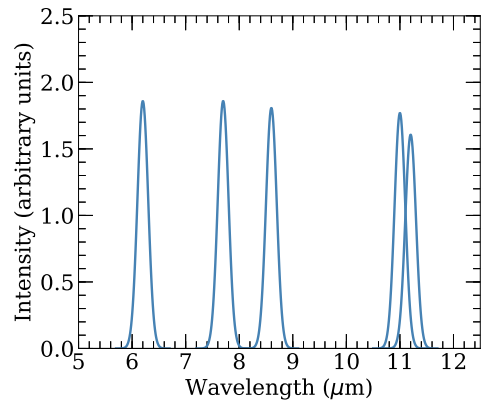


Figure 4. Eigen spectrum of PC_1 in NGC 2023. The eigen spectrum is an artificial spectrum created to visualize the contribution of a given PAH band to PC_1 (see text for details).

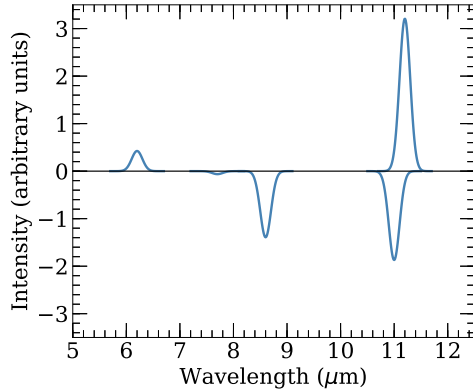


Figure 5. Eigen spectrum of PC_2 in NGC 2033. The eigen spectrum is an artificial spectrum created to visualize the contribution of a given PAH band to PC_2 (see text for details).

dicted by PC_1 , we only constructed an eigen spectrum of PC_2 from the standardized flux variables so that we can clearly identify the variations in the relative correction intensities of each of the PAH bands. Setting $PC_1 = 0$ and $PC_2 = 1$ in equation 5 results in the PAH band intensities corresponding to the eigen spectrum of PC_2 . We emphasize that since the PAH band intensities thus derived are the intensities of the standardized flux variables (with a mean of 0 and a standard deviation of 1), they can have negative values. The resulting eigen spectrum is illustrated in Fig. 5.

The intensities of the 8.6 and 11.0 μm bands are negative, whereas the 6.2 and 11.2 μm bands have positive intensities. The 7.7 μm band has almost no intensity. The fact that the 8.6 and the 11.0 μm bands behave differently than the 11.2 μm band suggests that PC_2 is dependent on the PAH ionization state. However, the fact that the 6.2 μm (strong in ionized PAHs) behave similar as the 11.2 μm PAH band (strong in neutral PAHs) is very surprising. Indeed, although the 6.2, 7.7, and 8.6 μm bands correlate very well with each other (see Peeters et al. 2017), their relative contribution to PC_2 is different with the 6.2 and 7.7 μm band having opposite contribution with respect to the 8.6 μm PAH band. This is further addressed in Section 6.

4.4 Correlations between PCs and PAH fluxes

To gain further insight into the characteristics of the PCs, we investigated the correlations of PC_1 and PC_2 with the PAH band fluxes and various PAH band ratios. Fig. 6 shows the observed correlations for PC_1 with these variables, and lists their Pearson correlation coefficients. Overall, PC_1 is well correlated with the individual PAH fluxes and the total PAH flux, albeit with considerable variation in the correlation coefficients. The best correlation is that of PC_1 with

PAH ratio	R-value	95% Confidence Interval
6.2/11.2	-0.8030	-0.7866 — -0.8184
7.7/11.2	-0.8217	-0.8066 — -0.8357
8.6/11.2	-0.8514	-0.8386 — -0.8632
11.0/11.2	-0.8601	-0.8480 — -0.8714

Table 3. 95% Confidence Interval of the correlation coefficient (R-value) of PC_2 with PAH ionization ratios.

the total charged PAH flux, i.e. the sum of the fluxes of ionized PAH bands (6.2, 7.7, 8.6, and 11.0 μm) with correlation coefficient of 0.995. This observation is in line with our previous conclusion of PC_1 tracing emission of a mixture of PAH molecules comprising more ionized PAH molecules than neutrals (we also present the spatial distribution of PC_1 in Appendix A which reinforces this conclusion). Furthermore, PC_1 does not correlate at all with any PAH band ratio. As an example of this, we show the correlation of PC_1 with the 6.2/11.2 band ratio.

We also note some “branching” in the correlation plots of PC_1 , i.e. there appears to be sets of data points that each correspond to slightly different relationships between parameters. The branching is most prominent in the correlation of PC_1 with the 11.2 μm band. Branches are also evident in the correlation of PC_1 with the 6.2 μm band and to some extent with the 11.0 and 8.6 μm bands as well. We will discuss the origin of these branches in Section 5.

Similar to PC_1 , we also investigated the correlations of PC_2 with individual band fluxes and various band ratios (Fig. 7). PC_2 does not correlate with individual PAH fluxes nor the total PAH flux. Instead, PC_2 anti-correlates best with 11.0/11.2, which is a measure of the PAH ionization state. This implies that high PC_2 values originate from more neutral regions and low PC_2 values originate from more cationic regions (see also the spatial distribution of PC_2 in Appendix A). PC_2 also anti-correlates well with other PAH ratios, the 8.6/11.2, 7.7/11.2, and 6.2/11.2 ratios, but with a decreasing correlation coefficient (ranging from R^2 : 0.7 to 0.6) in that order. The 11.0, 8.6, 7.7, and 6.2 μm bands are all attributed to ionized PAHs, so a ratio of any of these PAH fluxes with the 11.2 μm band traces the ionization state and thus a decrease in the correlation coefficient for these ionic bands requires further investigation. To test the statistical significance of this decrease in the correlation coefficient, we obtained the 95% confidence intervals (CIs) for each Pearson correlation coefficient (R-value) and checked if there is an overlap between those intervals (Table 3). The 95% CI of the correlation coefficient indicates that if we were to repeat our measurements of the PAH bands, we would find that 95% of the time, the correlation coefficient would fall within this interval. The calculated CIs follow the same trend as the correlation coefficients with a slight overlap between the CIs for 6.2/11.2 and 7.7/11.2 as well as for 8.6/11.2 and 11.0/11.2. We note that the CIs for 6.2/11.2 and 7.7/11.2 do not overlap with the CIs for 8.6/11.2 and 11.0/11.2. Thus the drop in the correlation coefficients of the PAH ionization ratios is not merely an anomaly by chance; rather, it hints towards systematically different behaviour of the ionic bands. We discuss this decrease in the correlation coefficient further in Section 6. In addition, we find (anti-) correlations of PC_2 with the other PAH band ratios which are not as tight as those tracing the charge state of PAHs. PC_2 shows a weak correlation with the 7.7/11.0, 6.2/11.0, 6.2/8.6, and 7.7/8.6 ratios. No (anti-) correlations are found between PC_2 and the 8.6/11.0 nor the 6.2/7.7 in our dataset.

5 Evidence for multiple PAH sub-populations

We now return to the branching observed in the correlations of the PCs with the PAH band fluxes (see Section 4.4). This

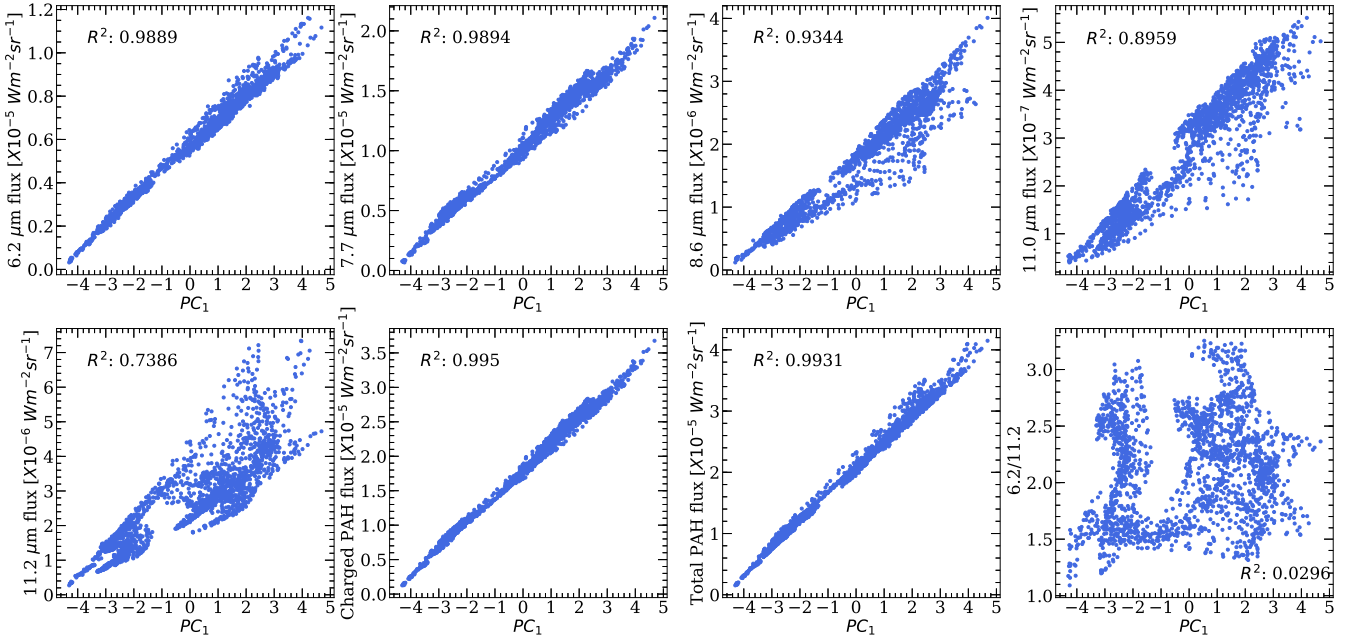


Figure 6. Correlations of PC_1 with the 6.2, 7.7, 8.6, 11.0, and 11.2 μm PAH band fluxes, the charged PAH flux, the total PAH flux, and the 6.2/11.2 ratio in NGC 2023. The Pearson correlation coefficient is shown at the top left corner of each plot. PC_1 is a dimensionless quantity representing the largest variance in the data set.

branching is most prominent in the correlation of PC_1 with the 11.2 μm . We show two such branches labelled as $B - 1$ and $B - 4$ in Fig. 8. A straight line in this correlation represents a set of data points with a specific relationship between the 11.2 μm PAH flux and the flux of the mixture of PAH molecules traced by PC_1 . The existence of these branches, i.e. a few sets of data points that each are characterized by their own 11.2/PAH flux as traced by PC_1 ratio, suggests that some of the properties of the underlying PAH populations are very similar within each of the branches, but different across the branches, and hence points towards the presence of distinct PAH sub-populations within the nebula.

In this section, we address the origin of these PAH sub-populations. In order to do so, we color coded the correlations of PC_1 with all possible PAH band ratios and checked which ratio sets the branches apart. We found that the 11.0/11.2 produces the cleanest separation of the branches (Fig. 8), thereby suggesting that the PAH sub-populations indicated by the branches in the correlation plot of PC_1 with the 11.2 μm are the result of the varying PAH ionization across the nebula. We note that while PC_2 has a strong correlation with the 11.0/11.2 PAH ratio, the branches are not the PAH emission variations traced by PC_2 . Due to the nature of the correlation between PC_2 and the 11.0/11.2 PAH ratio, PC_2 values show a relatively wide range of values within each of the branches, although the average value of PC_2 between the branches is different as well. To illustrate this, we show the dynamic range of PC_2 and 11.0/11.2 in two of the branches labelled $B - 1$ and $B - 4$ in Fig. 9. Note that the Fig. 9 is merely a sub-part of the PC_2 -11.0/11.2 plot shown in Fig. 7. While there are clear differences in ionization (as traced by PC_2) within a sub-population, their 11.0/11.2 ratio does not change much, and

thus the branches or sub-populations are best characterized based on the 11.0/11.2 PAH ratio rather than PC_2 .

There is a gradient in the 11.0/11.2 values across the correlation plots of PC_1 with the PAH band fluxes. In the PC_1 -11.2 plot, the high 11.0/11.2 values are at the lower part of the envelope of data points and the low 11.0/11.2 values are at the upper part of the envelope of data points as expected. This trend is reversed for the correlations of PC_1 with the 8.6 and 11.0, i.e. the high 11.0/11.2 values are at the upper part and the low 11.0/11.2 values are at the lower part of the envelope of data points. Surprisingly, this trend is not followed in the PC_1 -6.2 and the 7.7 plot, where there is an increased overlapping of the 11.0/11.2 values.

Since 11.0/11.2 traces the ionization state of PAHs, there is also a gradient of color, as expected, across the y-axis in the correlation plots of PC_1 with the 6.2/11.2, 7.7/11.2, and 8.6/11.2 PAH band ratios which are also the tracers of the PAH ionization. In addition, there is also an obvious gradient in the 11.0/11.2 values across the y-axis in the PC_1 -6.2/8.6, 7.7/8.6, 6.2/11.0, and 7.7/11.0 plots with high 11.0/11.2 values having low y-values and low 11.0/11.2 values having high y-values. In contrast, we do not observe any gradient in the PC_1 -6.2/7.7 and 8.6/11.0 plots. The presence of the gradient in the 6.2/8.6, 6.2/11.0, 7.7/8.6, and 7.7/11.0 PAH band ratios suggests that there is a distinction between the 6.2, 7.7 μm bands and the 8.6, 11.0 μm bands. The absence of any gradient in the 6.2/7.7 and the 8.6/11.0 ratios further suggests that the 6.2 and the 7.7 μm bands belong to one group of ionic bands and the 8.6 and the 11.0 μm belong to another. This is further addressed in the next Section.

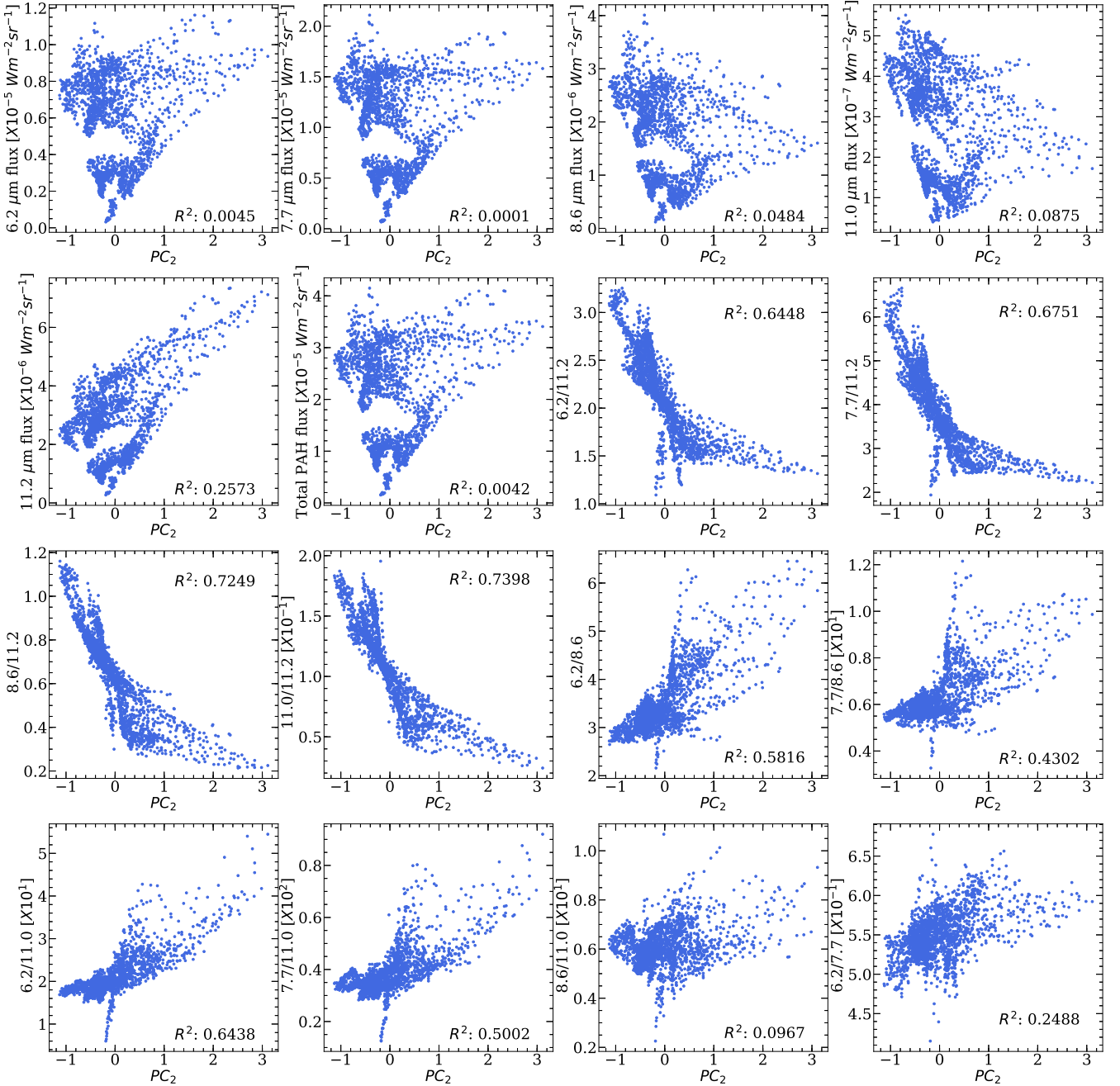


Figure 7. Correlations of PC_2 with the 6.2, 7.7, 8.6, 11.0, and 11.2 μm PAH band fluxes, the total PAH flux, and the various PAH band ratios across the south FOV in NGC 2023. The Pearson correlation coefficient is shown in the corner of the each plot. PC_2 is a dimensionless quantity representing the second largest variance in the data set.

6 Peculiar behaviour of the ionic bands

By now, we have encountered several instances that suggest that the ionic bands show different behaviour. First, there was the clear separation of the two sets of bands in the biplots. The characteristic spectrum of PC_2 furthermore shows a very peculiar behaviour of the ionic bands where we found that the behaviour of the 6.2 μm bears some similarity with that of the 11.2 μm , a neutral PAH band, while the other ionized PAH bands do not show such similarity. This behaviour is also reflected in the correlation of PC_2 with the 11.0/11.2, 8.6/11.2, 7.7/11.2, and the 6.2/11.2, where the

correlation coefficient decreases in this order, in spite of the 6.2, 7.7, 8.6, and 11.0 μm bands being attributed to ionized PAHs. Furthermore, the in-depth analysis of the branches seen in the correlations of PC_1 and PC_2 reveals that the 6.2 and 7.7 μm bands behave as one group of ionized bands and the 8.6 and 11.0 μm bands as another group.

The subtle behaviour of the ionic bands has been recognized previously by several authors (e.g. [Galliano et al. 2008](#); [Whelan et al. 2013](#); [Stock et al. 2014](#); [Peeters et al. 2017](#)). Numerous studies in the literature show that the correlation between the 6.2 and 7.7 μm bands is stronger

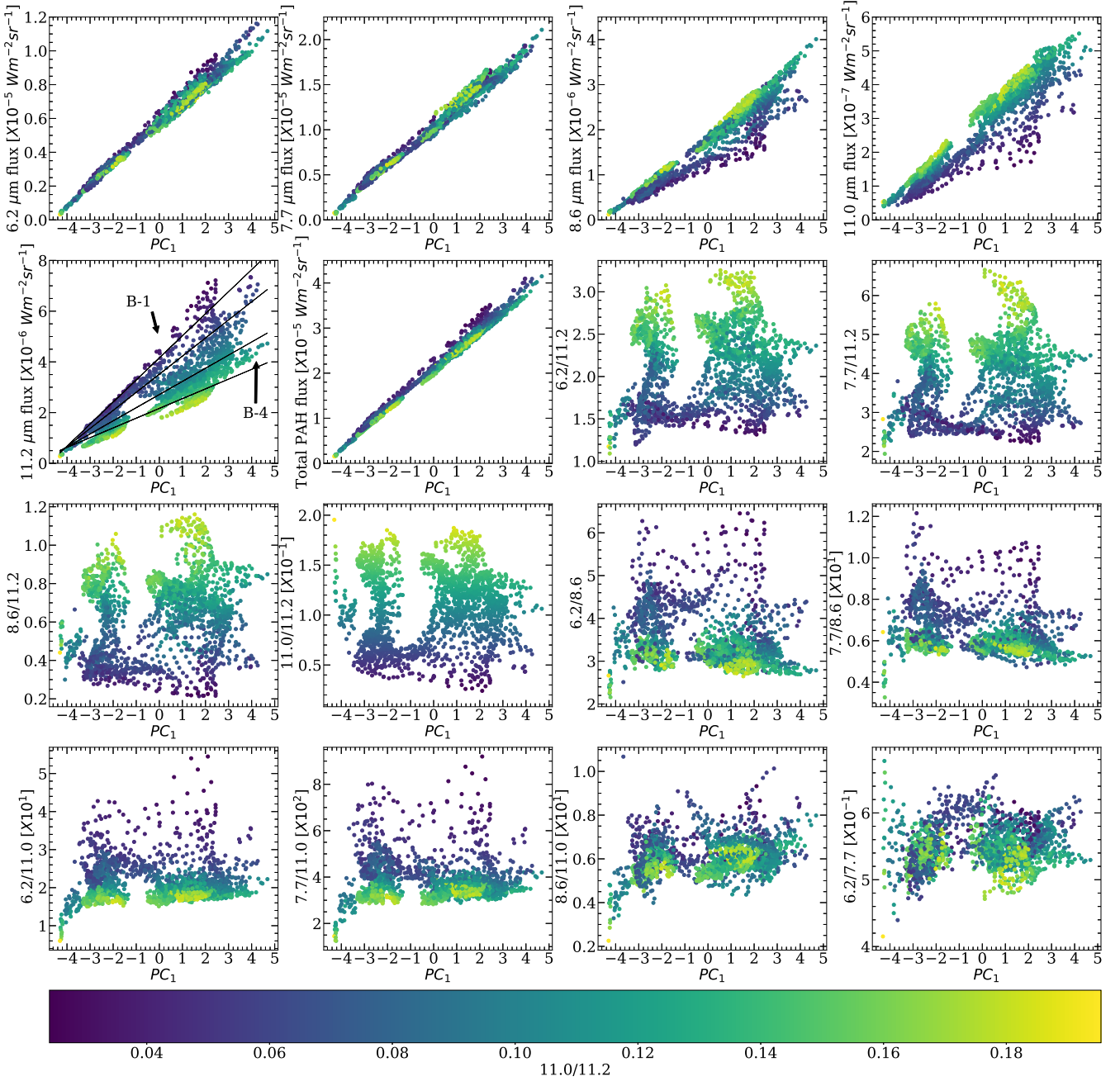


Figure 8. Correlations of PC_1 with the PAH band fluxes and the PAH band ratios color coded based on the 11.0/11.2 ratio to study the origin of the branches, most evident in the PC_1 - 11.2 correlation (see Section 4.4 for details).

than the correlation between the 6.2 or 7.7 and 8.6 μm bands (e.g. Vermeij et al. 2002; Galliano et al. 2008; Peeters et al. 2017; Maragkoudakis et al. 2018). Recently, Whelan et al. (2013) and Stock et al. (2014) observed the breakdown between the 6.2 and 7.7 μm bands in two HII regions in the Small Magellanic Cloud and in the Milky Way respectively. Furthermore, the broad 7.7 μm band is known to have at least two components at 7.6 and 7.8 μm (e.g. Bregman et al. 1989; Cohen et al. 1989; Verstraete et al. 2001; Peeters et al. 2002; Bregman & Temi 2005). Rapacioli et al. (2005) argue that the component at 7.8 μm is due to very small grains (VSGs). More recently,

Bouwman et al. (2019) studied the effect of size, symmetry and structure on the infrared spectra of four PAH cations and noted a drastic change in the vibrational modes of 7–9 μm region upon the decrease of the molecular symmetry (see also Bauschlicher et al. 2009).

Peeters et al. (2017) did a detailed analysis of emission in the 7–9 μm region in NGC 2023. They decomposed the spectrum in the 7–9 μm region into four Gaussian components. These authors found that two of the components centered at 7.6 and 8.6 μm correlate with each other and with the 11.0 μm band. These Gaussian components were the main contributors to the traditional 7.7 and 8.6 μm band in-

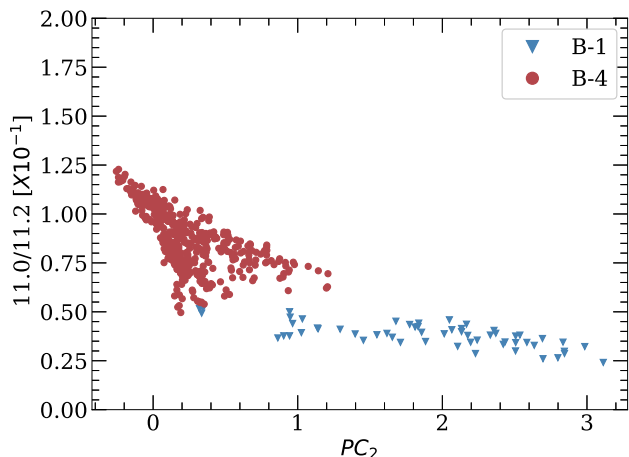


Figure 9. Range of PC_2 and 11.0/11.2 PAH ratio values within two branches (sub-populations) in NGC 2023.

tensities. The remaining two Gaussian components centered at 7.8 and 8.2 μm correlated with each other and displayed a spatial morphology similar to the 11.2 μm band and the 5–10 and 10–15 μm plateau emission in the south FOV and to the 10–15 μm plateau and the 10.2 μm continuum emission in the North FOV of NGC 2023. Despite the apparent arbitrariness of the decomposition, their results suggested the presence of at least two distinct sub-populations contributing to the emission in the 7–9 μm region. In this scenario, the contribution from the Gaussian component at 7.8 μm to the 7.7 μm complex is at the origin of the distinction observed between the 7.7 and 8.6 μm bands detected by the PCA analysis. Thus, the analysis presented here does not explicitly separate the two different PAH populations as suggested by Peeters et al. (2017) in their decomposition of the 7–9 μm region, rather it provides additional supporting evidence for their existence. Furthermore, our result that the 6.2 and 7.7 μm bands belong to a single group (as opposed to the 8.6/11.0 group), suggests that, similar to the 7.7 μm band, the 6.2 μm band contains contributions of both these two PAH populations responsible for the 7.7 μm band, which Peeters et al. (2017) were unable to extract using their analysis method. This is also supported by the fact that the correlation between the 6.2 and 7.7 μm bands is the strongest (e.g. Peeters et al. 2017).

We further notice that based on the correlations of PC_1 color-coded with the 11.0/11.2 ratio, the points with low values of 11.0/11.2 populate the regions of high values of 6.2/11.0, 7.7/11.0, 6.2/8.6, and 7.7/8.6. The fact that we see a color distinction in the ratios of these ionic bands due to an ionization ratio (11.0/11.2) itself may suggest that these ratios are further tracing the different ionization states of the PAH molecules. Since high values of 6.2/11.0, 7.7/11.0, 6.2/8.6, and 7.7/8.6 correspond to low values of 11.0/11.2, this then implies that the 6.2 and 7.7 μm bands originate from less ionized PAHs than the 8.6 and 11.0 μm bands. Thus, an alternative interpretation for the distinction between the two groups of the ionized bands is that the 6.2 and 7.7 μm trace singly charged PAH cations and the 8.6 and 11.0 μm trace doubly charged PAH cations. We emphasize that based on previous

studies (e.g. Bauschlicher et al. 2009; Peeters et al. 2017; Bouwman et al. 2019; Maragkoudakis et al. 2018, 2020), other PAH properties such as size and molecular structure are known to influence the PAH emission spectrum. Maragkoudakis et al. (2020) have shown that PAH size primarily effect the 3.3 μm band and to a lesser extent the 11.2 μm band indicating that size is likely not the driver of the observed dichotomy between the ionic bands. The effect of molecular structure on these ionic bands in terms of band assignments has been discussed in Peeters et al. (2017). However, we currently can not systematically investigate its role within this context based on the astronomical observations.

7 The PCs and the physical conditions

The primary goal of a PCA is to reduce the set of parameters needed to represent a multivariate data set and find the key variables that drive the input data. By performing a PCA of five PAH band fluxes in NGC 2023, we find that only two variables (PCs) are required to explain $\sim 99\%$ of the variance in the PAH emission in NGC 2023. Based on the characteristic spectrum of the PCs and their correlations, we conclude that i) PC_1 representing the largest variance represents the PAH emission of an ion dominated PAH mixture, and ii) PC_2 constituting the second largest variance has a strong (anti)-correlation with the PAH band ratios, 6.2/11.2, 7.7/11.2, 8.6/11.2, and 11.0/11.2, tracing the ionization state of the PAHs, and a moderate to weak correlation with the 7.7/11.0, 6.2/11.0 and the 6.2/8.6, 7.7/8.6 respectively. In this section, we now explore if there is a relation between the PCs and the parameters that describe the physical conditions in the nebula. Note that the key physical parameters that determine the PAH emission characteristics are the strength of the radiation field, the PAH abundance, electron density, and the temperature. We focus here on the radiation field strength distribution.

We note that the spatial morphology of $-PC_2$ resembles that of G_0 in the north and south FOVs of NGC 2023 (see Fig. C1) with $-PC_2$ exhibiting high values in the high G_0 regions closer to the star (i.e at the bottom of the north FOV and the top of the south FOV) and vice versa. This similarity highlights the influence of G_0 on PC_2 . Although PC_1 also exhibits maxima in the high G_0 regions (S' and SE ridge in south FOV; west of the southern part of the NW ridge), the overall morphology of PC_1 and G_0 is very different in both FOVs (see Figs. A1 and C1). Thus we conclude that, variations in the PAH emission reflected by PC_2 are strongly affected by G_0 , this seems to be less so for PC_1 . We also compared the spatial distribution of PCs to that of G_0/n_H , where n_H is the local hydrogen density. Fleming et al. (2010) presented the map of G_0/n_H estimated from the ionization state of the PAHs for the south FOV. We find no morphological similarity in the maps of PCs and G_0/n_H (see Fig. 6 in Fleming et al. 2010).

In Section 4.4, we noted that PC_2 correlated well with the ratios of ionic PAH bands, 6.2/8.6, 7.7/8.6, 6.2/11.0, and 7.7/11.0 (see Figs. 7), which reflects the distinction between the two groups of ionic PAH bands. Since G_0 affects PC_2 values, one could conclude that the distinction between these two groups of ionic bands is driven by G_0 . This also extends support to our hypothesis that the 8.6 and 11.0 μm

band could be tracing dications as one would expect more doubly charged cations than singly charged cations in high G_0 regions corresponding to low PC_2 values and hence low values of 6.2/8.6, 7.7/8.6, 6.2/11.0, and 7.7/11.0 which is indeed the case.

8 Conclusion

We have presented a principal component analysis of the fluxes of five major PAH features at 6.2, 7.7, 8.6, 11.0, and 11.2 μm in the south and the north FOV of NGC 2023. We find that only two principal components (PCs) are required to explain 99% of the variance in the fluxes of the five PAH bands considered here. Out of the two components, the first PC (PC_1) is the most important component as it carries the majority (91%) of the information about the data.

In order to interpret the characteristics of the PCs, we studied their characteristic PAH spectrum, eigen spectrum, and the correlations with the individual PAH band fluxes and PAH band ratios. Based on these we concluded that PC_1 represents the PAH emission of a mixture of molecules having more ionized PAHs than neutral PAHs and PC_2 traces the ionization state of PAH molecules. In addition, the correlations of PCs with PAH band fluxes revealed distinct “branches” which indicated the presence of multiple PAH sub-populations due to varying PAH ionization across the nebula.

Based on the eigen spectrum of PC_2 and its correlations with the ionic PAH band ratios, we find that there is a distinction between the ionic PAH bands, with the 6.2 and 7.7 μm bands and the 8.6 and 11.0 μm bands belonging to two different groups of ionized bands. We further argue that the 6.2 and 7.7 μm bands originate from less ionized PAHs than the 8.6 and 11.0 μm bands and thus the 6.2 and 7.7 μm bands could be attributed to singly charged PAH cations and the 8.6 and 11.0 μm bands to doubly charged PAH cations. Furthermore, the comparison of PCs with the physical conditions in the nebula shows that the spatial map of $-PC_2$ is similar to that of G_0 , and hence we concluded that the G_0 drives the distinction observed between the ionic bands.

Data Availability

The data underlying this article are available at <https://github.com/Ameeek-Sidhu/PCA-NGC2023>.

Acknowledgements

The authors thank the referee for providing valuable comments which led to the improvement of this paper. EP and JC acknowledge support from an NSERC Discovery Grant.

REFERENCES

Abdi, H., & Williams, L. J. 2010, Wiley Interdisciplinary Reviews: Computational Statistics, 2, 433
 Abergel, A., et al. 2002, A&A, 389, 239
 —. 2010, A&A, 518, L96

Allamandola, L. J., Hudgins, D. M., & Sandford, S. A. 1999, ApJ, 511, L115
 Allamandola, L. J., Tielens, A. G. G. M., & Barker, J. R. 1985, ApJ, 290, L25
 —. 1989, ApJS, 71, 733
 Andrews, H., Peeters, E., Tielens, A. G. G. M., & Okada, Y. 2018, A&A, 619, A170
 Aniano, G., Draine, B. T., Gordon, K. D., & Sandstrom, K. 2011, PASP, 123, 1218
 Bauschlicher, Jr., C. W., Peeters, E., & Allamandola, L. J. 2008, ApJ, 678, 316
 —. 2009, ApJ, 697, 311
 Berné, O., & Tielens, A. G. G. M. 2012, Proceedings of the National Academy of Science, 109, 401
 Berné, O., et al. 2007, A&A, 469, 575
 Black, J. H., & van Dishoeck, E. F. 1987, ApJ, 322, 412
 Boersma, C., Bregman, J., & Allamandola, L. J. 2015, ApJ, 806, 121
 —. 2016, ApJ, 832, 51
 —. 2018, ApJ, 858, 20
 Bouwman, J., Castellanos, P., Bulak, M., Terwisscha van Scheltinga, J., Cami, J., Linnartz, H., & Tielens, A. G. G. M. 2019, A&A, 621, A80
 Bregman, J., & Temi, P. 2005, ApJ, 621, 831
 Bregman, J. D., Allamandola, L. J., Witteborn, F. C., Tielens, A. G. G. M., & Geballe, T. R. 1989, ApJ, 344, 791
 Burton, M. G., Howe, J. E., Geballe, T. R., & Brand, P. W. J. L. 1998, Publ. Astron. Soc. Australia, 15, 194
 Candian, A., Sarre, P. J., & Tielens, A. G. G. M. 2014, ApJ, 791, L10
 Cesarsky, D., Lequeux, J., Ryter, C., & Gérin, M. 2000, A&A, 354, L87
 Cohen, M., Tielens, A. G. G. M., Bregman, J., Witteborn, F. C., Rank, D. M., Allamandola, L. J., Wooden, D., & Jourdain de Muizon, M. 1989, ApJ, 341, 246
 Croiset, B. A., Candian, A., Berné, O., & Tielens, A. G. G. M. 2016, A&A, 590, A26
 Draine, B. T., & Bertoldi, F. 1996, ApJ, 468, 269
 Field, D., Gerin, M., Leach, S., Lemaire, J. L., Pineau Des Forets, G., Rostas, F., Rouan, D., & Simons, D. 1994, A&A, 286, 909
 Fleming, B., France, K., Lupu, R. E., & McCandliss, S. R. 2010, ApJ, 725, 159
 Galliano, F., Madden, S., Tielens, A., Peeters, E., & Jones, A. 2008, ApJ, 679, 310
 Hony, S., Van Kerckhoven, C., Peeters, E., Tielens, A. G. G. M., Hudgins, D. M., & Allamandola, L. J. 2001, A&A, 370, 1030
 Hotelling, H. 1933, Journal of Educational Psychology, 24, 417
 Houck, J. R., et al. 2004, ApJS, 154, 18
 Hudgins, D. M., & Allamandola, L. J. 1999, ApJ, 516, L41
 Joblin, C., Tielens, A. G. G. M., Geballe, T. R., & Wooden, D. H. 1996, ApJ, 460, L119
 Jolliffe, I. T., & Cadima, J. 2016, Philosophical Transactions of the Royal Society of London Series A, 374, 20150202
 Kaufman, M. J., Wolfire, M. G., Hollenbach, D. J., & Luhman, M. L. 1999, ApJ, 527, 795
 Knight, C., Peeters, E., Tielens, A., & Stock, D. 2019, submitted
 Kounkel, M., et al. 2018, AJ, 156, 84
 Leger, A., & Puget, J. L. 1984, A&A, 137, L5
 Li, A., & Draine, B. T. 2001, ApJ, 554, 778
 Maragkoudakis, A., Ivkovich, N., Peeters, E., Stock, D. J., Hemachandra, D., & Tielens, A. G. G. M. 2018, MNRAS, 481, 5370
 Maragkoudakis, A., Peeters, E., & Ricca, A. 2020, MNRAS, 494, 642
 Meixner, M., Haas, M. R., Tielens, A. G. G. M., Erickson, E. F., & Werner, M. 1992, ApJ, 390, 499
 Pearson, K. 1901, Philosophical Magazine Series 6, 2, 559

- Peeters, E., Bauschlicher, Jr., C. W., Allamandola, L. J., Tielens, A. G. G. M., Ricca, A., & Wolfire, M. G. 2017, *ApJ*, 836, 198
- Peeters, E., Hony, S., Van Kerckhoven, C., Tielens, A. G. G. M., Allamandola, L. J., Hudgins, D. M., & Bauschlicher, C. W. 2002, *A&A*, 390, 1089
- Peeters, E., Tielens, A. G. G. M., Allamandola, L. J., & Wolfire, M. G. 2012, *ApJ*, 747, 44
- Pilleri, P., Montillaud, J., Berné, O., & Joblin, C. 2012, *A&A*, 542, A69
- Poglitsch, A., et al. 2010, *A&A*, 518, L2
- Rapacioli, M., Joblin, C., & Boissel, P. 2005, *A&A*, 429, 193
- Ricca, A., Bauschlicher, Jr., C. W., Boersma, C., Tielens, A. G. G. M., & Allamandola, L. J. 2012, *ApJ*, 754, 75
- Roche, P. F., Aitken, D. K., & Smith, C. H. 1989, *MNRAS*, 236, 485
- Rosenberg, M. J. F., Berné, O., Boersma, C., Allamandola, L. J., & Tielens, A. G. G. M. 2011, *A&A*, 532, A128
- Sandell, G., Mookerjee, B., Güsten, R., Requena-Torres, M. A., Riquelme, D., & Okada, Y. 2015, *A&A*, 578, A41
- Schutte, W. A., Tielens, A. G. G. M., & Allamandola, L. J. 1993, *ApJ*, 415, 397
- Sellgren, K. 1984, *ApJ*, 277, 623
- Sellgren, K., Werner, M. W., & Dinerstein, H. L. 1983, *ApJ*, 271, L13
- Shannon, M. J., Stock, D. J., & Peeters, E. 2016, *ApJ*, 824, 111
- Sheffer, Y., Wolfire, M. G., Hollenbach, D. J., Kaufman, M. J., & Cordier, M. 2011, *ApJ*, 741, 45
- Sloan, G. C., Hayward, T. L., Allamandola, L. J., Bregman, J. D., Devito, B., & Hudgins, D. M. 1999, *ApJ*, 513, L65
- Smith, J. D. T., et al. 2007, *ApJ*, 656, 770
- Steiman-Cameron, T. Y., Haas, M. R., Tielens, A. G. G. M., & Burton, M. G. 1997, *ApJ*, 478, 261
- Stock, D. J., Choi, W. D. Y., Moya, L. G. V., Otaguro, J. N., Sorkhou, S., Allamandola, L. J., Tielens, A. G. G. M., & Peeters, E. 2016, *ApJ*, 819, 65
- Stock, D. J., & Peeters, E. 2017, *ApJ*, 837, 129
- Stock, D. J., Peeters, E., Choi, W. D. Y., & Shannon, M. J. 2014, *ApJ*, 791, 99
- Vermeij, R., Peeters, E., Tielens, A. G. G. M., & van der Hulst, J. M. 2002, *A&A*, 382, 1042
- Verstraete, L., et al. 2001, *A&A*, 372, 981
- Werner, M. W., et al. 2004, *ApJS*, 154, 1
- Whelan, D. G., Lebouteiller, V., Galliano, F., Peeters, E., Bernard-Salas, J., Johnson, K. E., Indebetouw, R., & Brandl, B. R. 2013, *ApJ*, 771, 16
- Witt, A. N., Schild, R. E., & Kraiman, J. B. 1984, *ApJ*, 281, 708
- Wolfire, M. G., Tielens, A. G. G. M., & Hollenbach, D. 1990, *ApJ*, 358, 116

Appendix

A Spatial Maps of PCs

It is insightful to create maps of the variations in PC_1 and PC_2 and compare those to spatial maps of PAH features described in Peeters et al. (2017). Fig. A1 shows the spatial distribution of PC_1 and PC_2 in the north and the south FOV. In order to facilitate comparison with the spatial maps of PAH features in Peeters et al. (2017), we show the contours of the 7.7 and 11.2 μm PAH bands at the same intensity levels as chosen by Peeters et al. (2017), i.e. at 1.40, 1.56, 1.70, and $1.90 \times 10^{-5} \text{ Wm}^{-2}\text{sr}^{-1}$ and 3.66, 4.64, 5.64, and $6.78 \times 10^{-6} \text{ Wm}^{-2}\text{sr}^{-1}$ respectively. Moreover, we annotate the ridges as defined by Peeters et al. (2017) in the two FOVs.

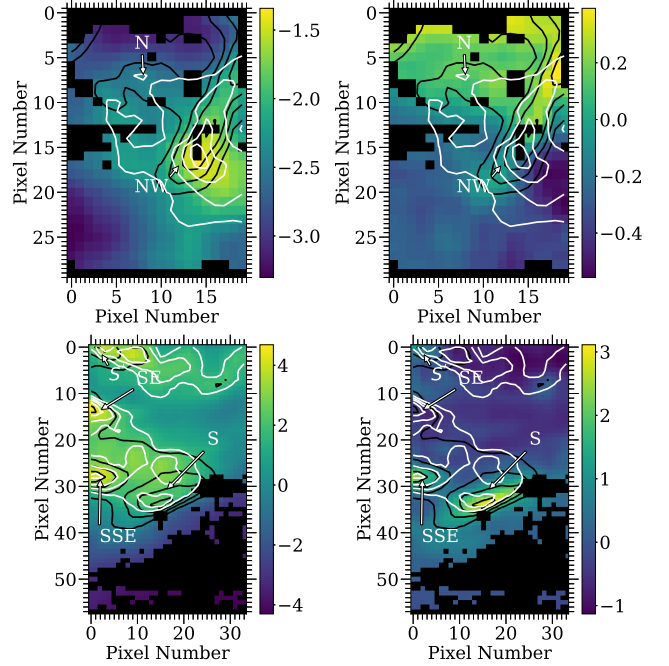


Figure A1. Spatial map of PC_1 (left) and PC_2 (right) in the north (top) and the south (bottom) FOV of NGC 2023. For reference, the ridges as defined by Peeters et al. (2017) are annotated and the contours of the intensity of the 7.7 and 11.2 μm PAH bands are shown in white and black respectively. Pixels without 3 σ detection for all five PAH bands and containing the YSOs C and D from Sellgren et al. (1983) are masked from the analysis and are shown in black.

To first order, the spatial morphology of PC_1 is very similar to the map of total PAH flux (see Figs. 5 and 6 in Peeters et al. 2017). However, there are subtle differences. In the south FOV, the total PAH emission peaks at S', SE, SSE, and S ridges with the S', SE, and SSE ridges being dominated by cations and the S ridge by neutral PAHs (Peeters et al. 2017). PC_1 peaks at S', SE, and SSE ridges but not at the S ridge. In the S ridge, PC_1 values are high, but do not exhibit a maximum. In addition, PC_1 is strong at the broad, diffuse plateau north and north-west of the S and SSE ridges, where strong emission is also observed from the 8.6 and 11.0 μm PAH emission bands (Peeters et al. 2017). In the north FOV, the total PAH flux peaks on the NW ridge, while PC_1 , although high in the NW ridge, peaks slightly west of the southern part of the NW ridge, where emission from PAH cations peak. Thus, the spatial morphology of PC_1 in two FOVs shows that PC_1 peaks in the cation dominated ridges and is high but does not peak in the neutral dominated ridges. This lends further support to our conclusion about PC_1 that it represents emission of a mixture of PAH molecules with more ionized PAHs than the neutral PAHs.

PC_2 peaks at the S and the SSE ridge in the south FOV. In all regions other than the S, SSE and a part of the S' ridge, PC_2 is negative and seemingly uniform. The spatial morphology of PC_2 resembles that of the H₂ 9.7 μm S(3) and 12.3 μm S(2) line intensities (see Fig 5 in Peeters et al. 2017). In the north FOV, PC_2 peaks at the north part of

the NW ridge and has a sub-dominant emission in the center part of the N ridge where its projection connects with the NW ridge. PC_2 exhibits a minimum in the regions south of the N and the NW ridge and west of the southern part of the NW ridge, which are closer to the illuminating star. Its spatial morphology seems to fall between that of the 10-15 μm plateau and the 11.2 μm PAH emission. The fact that PC_2 exhibits a maximum in the neutral dominated ridges and a minimum in the cation dominated regions reinforces the suggestion that PC_2 is a quantity related to the ionization state of the PAHs.

B Methodology: Spatial map of radiation field strength

The intensity of the radiation field, G_0 , can be determined indirectly from observations of the FIR continuum emission or the H_2 rotation-vibration lines (e.g. Meixner et al. 1992; Black & van Dishoeck 1987; Draine & Bertoldi 1996; Burton et al. 1998; Sheffer et al. 2011). It can also be estimated indirectly based on PDR models combined with observations of the FIR cooling lines (e.g. Wolfire et al. 1990; Kaufman et al. 1999; Sandell et al. 2015). These methods, however, are limited in spatial resolution. Alternatively, we can estimate G_0 from empirical calibrations where G_0 is first estimated from other methods and then calibrated against some suitable dust grain or PAH parameter (e.g. Pilleri et al. 2012; Stock & Peeters 2017). Here, we obtained the maps of G_0 for NGC 2023 using the empirical calibrations of Stock & Peeters (2017) and Pilleri et al. (2012) (hereafter referred to as method 1 and method 2 respectively) and from observations of the FIR continuum emission (referred as method 3 in the remaining of the paper). These three methods are described in detail below.

Method 1: We derived the morphology of radiation field strength (G_0) using the empirical relationship established between G_0 and the ratio of two subcomponents (7.6 and 7.8) of the 7.7 μm feature by Stock & Peeters (2017). These subcomponents are two of the four Gaussian components, approximately centered at 7.6, 7.8, 8.2, and 8.6 μm , used by Peeters et al. (2017) to better fit the features in the 7-9 μm region. Based on a sample of Galactic H II regions and reflection nebulae, Stock & Peeters (2017) found the following relationship between G_0 and the 7.8/7.6 ratio:

$$I_{7.8}/I_{7.6} = (1.70 \pm 0.13) - (0.28 \pm 0.03) \log G_0 \quad (\text{B1})$$

We note that the south FOV of NGC 2023 was in the sample used by Stock & Peeters (2017) to derive equation B1. These authors used slightly different values of central wavelength and full width at half maximum than Peeters et al. (2017) to decompose the features in the 7-9 μm region into the four Gaussian components. Thus, to derive the map of G_0 in the south FOV we used the fluxes of the 7.6 and 7.8 μm bands obtained from the decomposition parameters of Stock & Peeters (2017). The north FOV of NGC 2023 was not part of the sample used by Stock & Peeters (2017). We therefore obtained the fluxes of the 7.6 and 7.8 μm bands for this FOV using the average decomposition parameters for the reflection nebulae given by Stock & Peeters (2017).

Method 2: The second method used to derive the G_0 map is based on another empirical relation reported by

Pilleri et al. (2012). These authors found a strong anti-correlation between G_0 and the fraction of carbon locked in evaporating Very Small Grains (f_{eVSG}). eVSGs are carbonaceous grains having a wide size distribution (Li & Draine 2001). It is thought that photo-evaporation of these grains by UV photons lead to the formation of free gas-phase PAH molecules and hence the name eVSGs (Cesarsky et al. 2000; Rapacioli et al. 2005; Berné et al. 2007). Based on a sample of PDRs, Pilleri et al. (2012) found the following relation:

$$f_{\text{eVSG}} = (-0.23 \pm 0.02) \log G_0 + (1.21 \pm 0.05) \quad (\text{B2})$$

which is reliable in the range of G_0 from 100 to 5×10^4 .

We obtain f_{eVSG} from the decomposition method PAH-TAT, which fits the template spectra of neutral PAHs, ionized PAHs, cluster of PAHs, and eVSGs to the observed spectrum.

Method 3: The third method is based on the FIR continuum emission. This estimation of G_0 is based on the assumption that all FUV photons are absorbed by dust and re-radiated in the FIR. To measure the FIR flux density, we used the photometric images observed at 70 and 160 μm with the Herschel Photodetector Array Camera and Spectrometer (PACS, Poglitsch et al. (2010), AOR Key: 'PPhoto-ngc2023-135') from the Herschel Science Archive. The PACS 70 and 160 μm filters have pixel scales of 3.2" and 6.4" respectively. In order to achieve the same spatial resolution for both maps, we convolved the 70 μm image to the lower resolution 160 μm image using the convolution kernels and procedures from Aniano et al. (2011). Furthermore, these maps are constrained by the 3σ detection limit in the convolved 70 μm and 160 μm images.

The FIR flux density is then estimated by composing a spectral energy distribution (SED) and then fitting a modified blackbody function to the SED of the form

$$I(\lambda, T) = K/\lambda^\beta \times B(\lambda, T) \quad (\text{B3})$$

where K is a scaling parameter, β is the spectral index, and $B(\lambda, T)$ is the Planck Function as a function of the wavelength (λ) and the dust temperature (T) (e.g. Abergel et al. 2010; Berné & Tielens 2012; Andrews et al. 2018). To obtain the best fit, we fixed $\beta = 1.8$ and considered K and T to be the free parameters following previous analysis of similar regions (e.g. Berné & Tielens 2012; Andrews et al. 2018). The FIR flux is subsequently determined by integrating the area underneath the modified blackbody fit.

Subsequently, we determine G_0 from this FIR flux measurements following Meixner et al. (1992):

$$G_0 = 4\pi V l^{-1} S^{-1} \tau \lambda_0^\beta \int \lambda^{-\beta} B(\lambda, T) d\lambda \quad (\text{B4})$$

where V is the volume of the region, S the surface area of the cloud facing the illuminating star, l the pathlength along the line of sight, and τ the optical depth at the reference wavelength λ_0 . Assuming a spherical geometry for the cavity of NGC 2023 (e.g. Field et al. 1994), the geometry factor $V l^{-1} S^{-1}$ reduces to 1.0. Thus an estimate for G_0 is derived by multiplying the FIR flux calculated from equation B3 by a factor of 4π and converting the units to the Habing field. Note that, the $\tau \lambda_0^\beta$ term

in equation B4 is accounted for by the scaling parameter, K .

C Spatial maps of radiation field strength

Here, we compare the G_0 maps obtained from the three methods described in Appendix B with each other in order to have a consistent spatial picture of G_0 across the nebula. Figs. C1 and C2 shows the resulting spatial distributions of G_0 for the north and south FOV based on the three methods. In the south FOV, the absolute values of G_0 in units of Habing Field estimated from method 1 and method 3 ranges between 10^3 and 10^4 , while, those estimated from method 2 varies in the range of 10^3 and 10^5 . We emphasize that the G_0 values $> 5 \times 10^4$ obtained with method 2 are not reliable (Pilleri et al. 2012). The spatial morphology derived from these three methods is fairly similar in the south FOV with high values of G_0 in the upper half of the FOV containing the S' and the SE ridges and low values in the lower half of the FOV containing the SSE and the S ridges. In the north FOV, the absolute G_0 values obtained with method 1 and method 2 range from 10^3 to 10^5 , whereas those derived from method 3 are of the order of 10^3 . We note that the method 1 of estimating G_0 based on the 7.8/7.6 PAH band ratio is highly sensitive to the decomposition parameters of the 7-9 μm region. Therefore, the high values of G_0 in the north FOV obtained with method 1 are a consequence of the chosen decomposition parameters. Thus, we conclude that similar to method 2, the high G_0 values from method 1 are also not reliable in this FOV. Nevertheless, the similar spatial morphology of G_0 derived from method 1 and method 2 implies that there is a definite variation in G_0 across the FOV, with G_0 exhibiting a minimum in the upper part of the FOV containing the N and the northern part of the NW ridge, intermediate values in the south of the NW ridge and a maximum in the lower part of the FOV towards the star. However, due to the limitation in the spatial resolution, a similar conclusion about the spatial morphology could not be drawn for the G_0 map obtained with method 3. Thus, overall in the south FOV, the three methods of estimating G_0 are consistent with each other in terms of spatial distribution and the absolute values except for the high values of G_0 in method 2. On the other hand in the north FOV, the absolute G_0 values derived from these three methods are not comparable. While the information on spatial morphology of G_0 from method 3 could not be obtained, we find that method 1 and method 2 are consistent with each other in this FOV.

This paper has been typeset from a \LaTeX file prepared by the author.

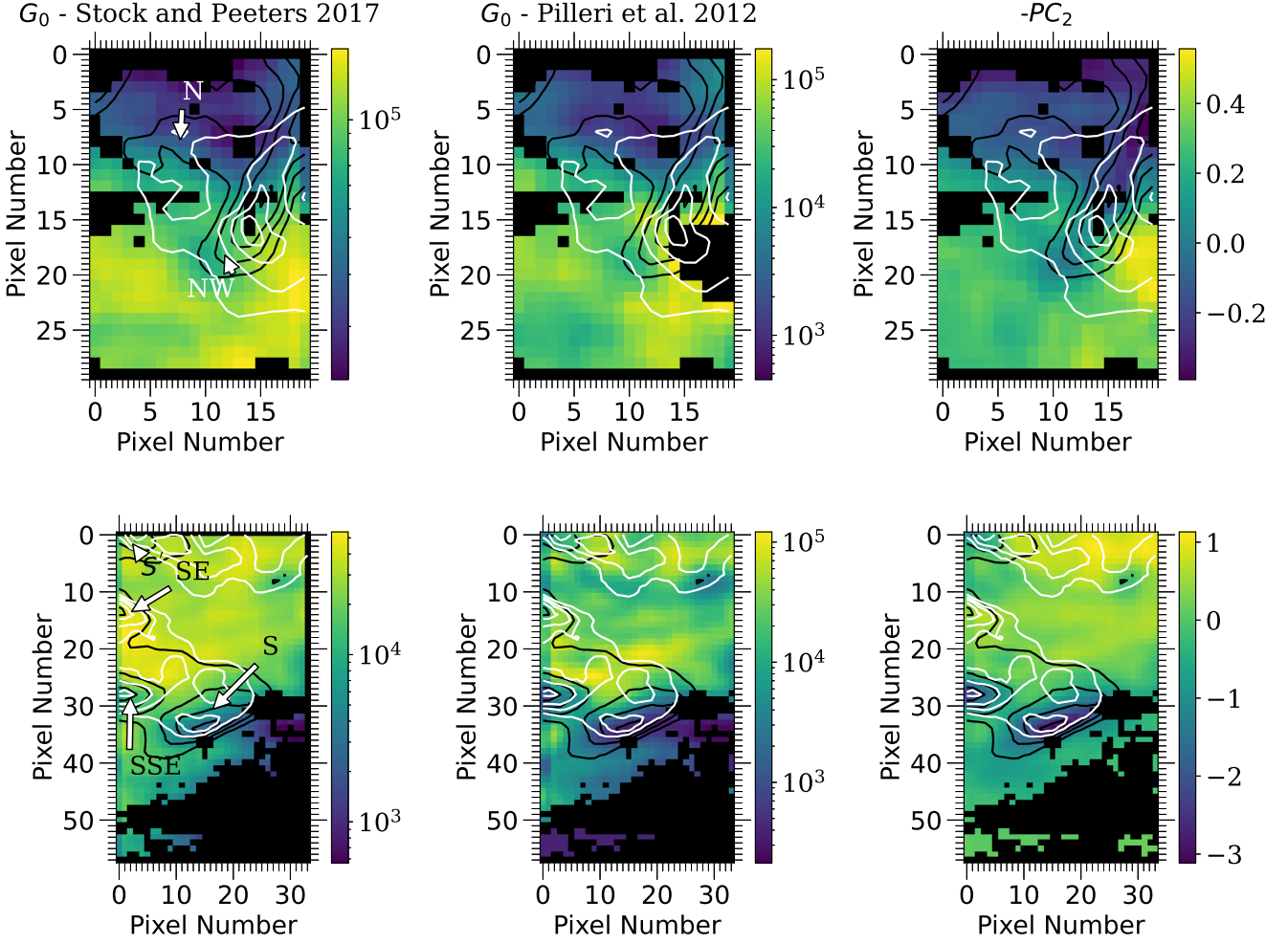


Figure C1. Spatial maps of G_0 in units of Habing Field derived from empirical calibrations across the north (top row) and the south (bottom row) FOV of NGC 2023. Left panel: G_0 derived from its correlation with the 7.8/7.6 PAH ratio given by Stock & Peeters (2017) in the logarithmic color scale. Pixels where the intensity of both 7.6 and 7.8 μm bands is zero are shown in black in addition to those masked while performing PCA; Middle panel: G_0 derived from its (anti)-correlation with eVSGs given by Pilleri et al. (2012) in the logarithmic color scale. Pixels where $f_{eVSG} = 0$ are shown in black in addition to those masked while performing PCA; Right panel: $-PC_2$ for comparison. Pixels masked while performing PCA are shown in black. For reference, the ridges as defined by Peeters et al. (2017) are annotated for the north and south FOV in left panels. The contours of the intensity of the 7.7 and 11.2 μm PAH bands are shown in white and black respectively.

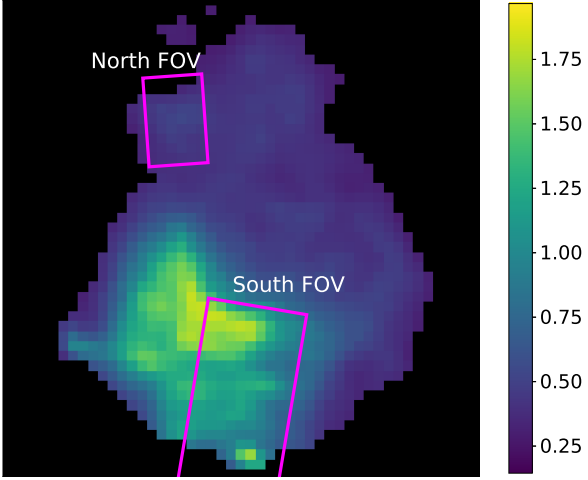


Figure C2. Spatial maps of G_0 in units of $10^4 \times$ Habing Field derived from the FIR continuum measurements (see Appendix B for details). North is up and East is to the left in the figure.